Research Article | Vol. 13, No. 10 / 1 Oct 2022 / Biomedical Optics Express 5418
Biomedical Optics EXPRESS

Intravascular optical coherence elastography

TIANSHI WANG,[1] TOM PFEIFFER,[2] ALI AKYILDIZ,[1,3] HELEEN M. M. VAN BEUSEKOM,[1] ROBERT HUBER,[2] ANTONIUS F. W. VAN DER STEEN,[1,4,5] AND GIJS VAN SOEST[1,*]

[1]*Thoraxcentre, Erasmus University Medical Centre, Rotterdam 3015 AA, The Netherlands*
[2]*Institut für Biomedizinische Optik, Universität zu Lübeck, Lübeck 23562, Germany*
[3]*Department of Biomechanical Engineering, Delft University of Technology, Delft 2600 AA, The Netherlands*
[4]*Shenzhen Institutes of Advanced Technology, Chinese Academy of Sciences, Shenzhen 518005, China*
[5]*Department of Imaging Science and Technology, Delft University of Technology, Delft 2600 AA, The Netherlands*
[*]*g.vansoest@erasmusmc.nl*

Abstract: Optical coherence elastography (OCE), a functional extension of optical coherence tomography (OCT), visualizes tissue strain to deduce the tissue's biomechanical properties. In this study, we demonstrate intravascular OCE using a 1.1 mm motorized catheter and a 1.6 MHz Fourier domain mode-locked OCT system. We induced an intraluminal pressure change by varying the infusion rate from the proximal end of the catheter. We analysed the pixel-matched phase change between two different frames to yield the radial strain. Imaging experiments were carried out in a phantom and in human coronary arteries *in vitro*. At an imaging speed of 3019 frames/s, we were able to capture the dynamic strain. Stiff inclusions in the phantom and calcification in atherosclerotic plaques are associated with low strain values and can be distinguished from the surrounding soft material, which exhibits elevated strain. For the first time, circumferential intravascular OCE images are provided side by side with conventional OCT images, simultaneously mapping both the tissue structure and stiffness.

1. Introduction

Optical coherence tomography (OCT) is a powerful tool for biomedical imaging and industrial non-destructive testing [1–4]. Two-dimensional (2D) or three-dimensional (3D) OCT images show in detail the microstructure of samples with a resolution of typically 10 µm and a penetration depth around 1 mm. Intravascular OCT (IV-OCT) has been developed to guide interventions in patients with coronary artery disease. An optical imaging catheter delivers the OCT light beam into the artery, directs it onto the artery wall and collects the back-reflected light for image reconstruction [3,5–7]. The typical diameter of the catheter is less than a millimetre, compatible with the small lumen size of the coronary vasculature.

Since the first demonstration of intracoronary imaging in a living patient in 2001 [8], IV-OCT has generated a wealth of insights into coronary artery diseases and stenting [6]. The number of IV-OCT–guided percutaneous coronary intervention (PCI) procedures was estimated to be approximately 100,000 per year in 2017, with a growth rate of 20% per year [9]. In clinical practice, tissue characterization using IV-OCT in coronary arteries affected by atherosclerosis can inform PCI decision-making [10,11]. Hard calcified plaque may impede full stent expansion and so lead to complications during and after the intervention, while soft and fragile lipid-rich plaque should be avoided as a stent-edge landing zone [6,12]. Presently, plaque composition is inferred from OCT image features, such as brightness or border definition [6], but the interpretation of OCT image features requires experience and may be affected by imaging artifacts [13,14]. Multimodal imaging techniques combine IV-OCT with, for instance, fluorescence or absorption

#470039 https://doi.org/10.1364/BOE.470039
Journal © 2022 Received 11 Jul 2022; revised 30 Aug 2022; accepted 31 Aug 2022; published 23 Sep 2022

Biomedical Optics EXPRESS

spectroscopy to improve tissue characterization [15–17]. Alternatively, functional extensions of OCT add tissue-type information by processing the OCT signal itself [18–20].

Intravascular ultrasound (IVUS)-based elastography has successfully characterized atherosclerotic plaque mechanics [21,22], and has been used to derive features that correlate with clinical aspects of coronary artery disease [23]. Optical coherence elastography (OCE), a functional extension of OCT, visualizes the strain in tissue to deduce the tissue's mechanical properties, which can support tissue characterization [24–27]. OCE involves inducing stress in tissue using a mechanical stimulus, detecting the displacement by processing the OCT data set and reconstructing the tissue strain to indicate the tissue stiffness qualitatively. An experimental demonstration of intravascular OCE (IV-OCE) imaging has so far remained elusive.

Elastography requires a mechanical stimulus to induce tissue strain. IVUS elastography uses the passive intracoronary pressure change as the stimulus, and the heart itself serves as the excitation pump [28,29]. Several studies attempted to integrate the excitation stimulus into the catheter itself, but the large dimension of the excitation source became an impediment to the catheter size [30].

Beam scanning stability is crucial to OCE analysis. Local tissue displacement at a sub-resolution scale induces a phase shift in the OCT signal. OCE extracts the phase shift by comparing the phase of two co-registered OCT frames, matched with subsample accuracy, acquired before and after the displacement [26,31]. In microscopic OCE, a frame-based phase comparison is guaranteed by the use of high-precision galvanometer scanning or an accurate moving stage to scan the sample. In a conventional catheter-based set-up, a proximal fibre joint rotates a long fibre probe. This scan mechanism is prone to non-uniform rotational distortion (NURD), complicating accurate alignment between two frames [7]. In contrast, distally actuated catheters use a micromotor at the catheter tip to implement a rotational scan [32–35], while the long fibre probe remains stationary during imaging. We have previously demonstrated that beam scanning stability can be significantly improved using a high-speed synchronous micromotor [36].

To bring OCE towards catheter-based applications, new solutions are needed. In this research, we demonstrate an experimental realization of phase-based OCE imaging of tissue strain in response to an applied stress by means of a side-looking, rotary scanning catheter. We characterize the method in an elastic tubular phantom and use it for IV-OCE of human coronary artery samples. The IV-OCE system integrated a 1.1 mm motorized catheter and a 1.6 MHz phase-sensitive Fourier domain mode-locked (FDML) OCT system. Stress is applied by modulating the fluid pressure in the lumen. A micromotor with a dual-layer coil design was developed specifically to enable stable beam scanning with the catheter, which allows us to compare the phase signal between two different frames sample by sample. At a frame rate of 3019 frames/s, the dynamic radial strain in response to a varying pressure can be measured by our IV-OCE system.

2. Methods

2.1. Dual-layered coil micromotor for stable beam scanning of the catheter

We developed a two-phase, two-pole synchronous micromotor that uses a structure of two separate coils etched on a flexible Kapton foil (Etchform BV, Hilversum, The Netherlands). Two channels of a sinusoid current signal with 90° phase shift were fed to the two layers of the coils. The widths of the copper tracks (Fig. 1(a)) were chosen to approximate a sinusoidal current distribution (Fig. 1(b)) by their relative resistance. The flexible print was rolled up inside a cylindrical stainless-steel housing (2.0×1.0 mm), forming a homogeneous magnetic field that rotates the magnetic rotor inside the housing. Compared to a single-layer design [36], this arrangement produces a more homogeneous field and consequently minimizes NURD (**Visualization 1**). We carried out a finite element model (FEM) simulation of the magnetic field (ANSYS, Maxwell 16.0) generated by the folded coil, which confirmed the uniformity of the

Biomedical Optics EXPRESS

produced field. More details of the magnetic field simulation can be found in Supplement 1 and in a video (**Visualization 1**). Based on the dual-layer micromotor, we developed an OCT catheter with 1.1 mm outer diameter (1.6 m length from tip). The design of the catheter can be found in our previous study [32], and the characterization of the catheter optics can be found in Supplement 1. The sine and cosine signals are supplied by an arbitrary waveform generator (AWG; Agilent 33522A; Santa Rosa, CA, USA) and converted to symmetric driving currents by a floating ground dual-channel balanced current amplifier.

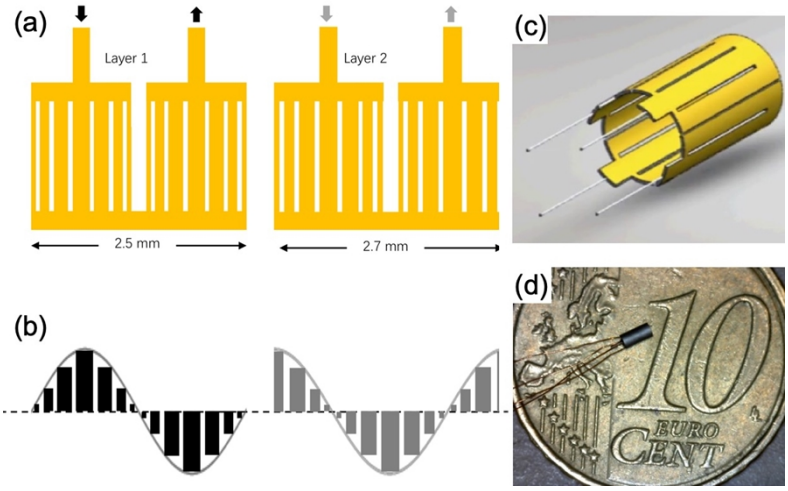

Fig. 1. (a) Schematic diagram of coils using dual-layer design. (b) Current density distribution in the coil. (c) The coils after rolling into a tube shape for assembly. (d) Photo of the dual-layer micromotor compared to a Euro coin of 10 cents.

2.2. Experimental set-up using motorized catheter

A photo of the motorized catheter is shown in Fig. 2. In IV-OCT used in clinical practice, a flexible tubular guiding catheter is used to deliver the flushing medium (physiological saline solution) and the imaging catheter to the coronary arteries. As shown in Fig. 2, the 1.1 mm motorized catheter was delivered to the lumen of the hollow imaging target through an 8-French guiding catheter (Boston Scientific, JR4) to realize circumferential cross-sectional imaging. Utilizing the stable scanning offered by the motorized catheter and the 1.6 MHz wavelength sweep rate of the FDML-based OCT engine, the IV-OCE system achieves an imaging speed of 3019 frames/s. The system's overall phase noise was 9.7 mrad, corresponding to a minimum detectable displacement of 0.76 nm. The maximum observable displacement without phase unwrapping corresponds to a phase shift of π rad, equivalent to 244 nm in tissue (refractive index $n_{ref} = 1.34$).

We controlled the intraluminal pressure by modifying the flush rate from the proximal end of the guiding catheter, which was positioned in the lumen of the imaged object. A home-built syringe pump was used to control both the volume and flush rate. The prescribed flush rate produced an elevated pressure in the lumen of the phantom or in the vessel because of the finite flow resistance in the tube; terminating the flow resulted in a gradually decaying pressure. The intraluminal pressure was monitored by a disposable in-line transducer (B. Braun, Melsungen, Germany).

Imaging experiments were performed in a polyvinyl alcohol (PVA) cryogel soft elastic tubular phantom with a stiff plastic (VeroWhitePlus; VWP) inclusion. The PVA hydrogel phantom was prepared with three freeze-thaw cycles and had an estimated Young's modulus of 100–150 kPa

Biomedical Optics EXPRESS

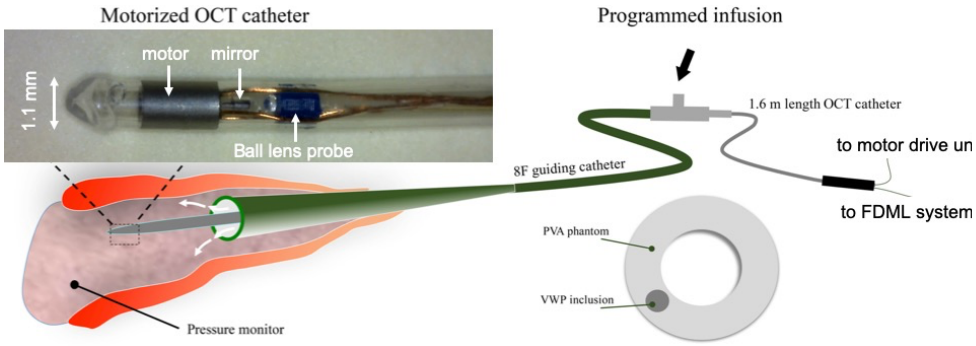

Fig. 2. Schematic diagram of the experimental set-up, shown with a photo of the motorized catheter, and cross-sectional diagram of the imaging phantom. PVA: poly(vinyl alcohol), VWP: VeroWhitePlus. The catheter is positioned via a guiding catheter, through which the flush media is delivered at a prescribed flow rate (white arrows) for pressure application.

[37]. A 2.5 mm lumen was formed by a mould, and a stiff inclusion made of VWP was implanted in the phantom to create a stiff area with a diameter of approximately 0.8 mm. The VWP material was chosen because its optical scattering is close to that of the PVA phantom, but it has a much larger Young's modulus of approximately 1400 MPa [38]. Thus, there was a large contrast in stiffness compared to the surrounding material but a similar OCT appearance.

2.3. Beam scanning and acquisition synchronization

The OCT system was built based on a phase-sensitive FDML laser [39,40]. The FDML laser cavity produces a master sweep at a frequency of 389460 Hz with a duty cycle of 25%. This master sweep is converted to a cluster output of one master sweep and three buffered copies, thus achieving a sweep rate of 1.6 MHz. More details of the FDML laser and the OCT system were previously described [41,42]; the characterization of the system can be found in Supplement 1.

We realized accurate frame-to-frame sample co-registration, required for phase analysis, by synchronizing the beam scanning, laser output, and data acquisition. Particularly, we programmed the motor drive signal using the FDML master sweep trigger, which also triggers the data acquisition. To form a circumferential image consisting of 516 A-lines, we discretized a sinusoidal cycle in 129 samples and applied the FDML master sweep trigger as an AWG sample clock. Figure 3 shows the timing sequence. In such way, corresponding A-lines (the white lines in Fig. 3) from two different frames will correspond to the same angular location, thus enabling a phase comparison. This combination of parameters leads to a speed of the micromotor of 3019 revolution/s and a frame rate of 3019 frames/s.

2.4. Signal processing and image construction

OCT data was acquired as wavelength-swept interferograms. After compensating the sampling offsets between master and buffered fringes and linearization in wavenumber domain, a fast Fourier transform was performed to convert the interferogram from the wavenumber domain to a complex data set I in the spatial domain, thus forming an A-line in a complex format [43]. Each set of 516 A-lines forms a circumferential cross-sectional frame. The absolute signal was used to construct the conventional structural OCT image, and the phase signal was processed for the OCE imaging.

We compute the strain image as follows, working in the polar domain. The local displacement d at sample j in A-line i can be measured by extracting the phase shift $\Delta\varphi$ between frame (f) and

Biomedical Optics EXPRESS

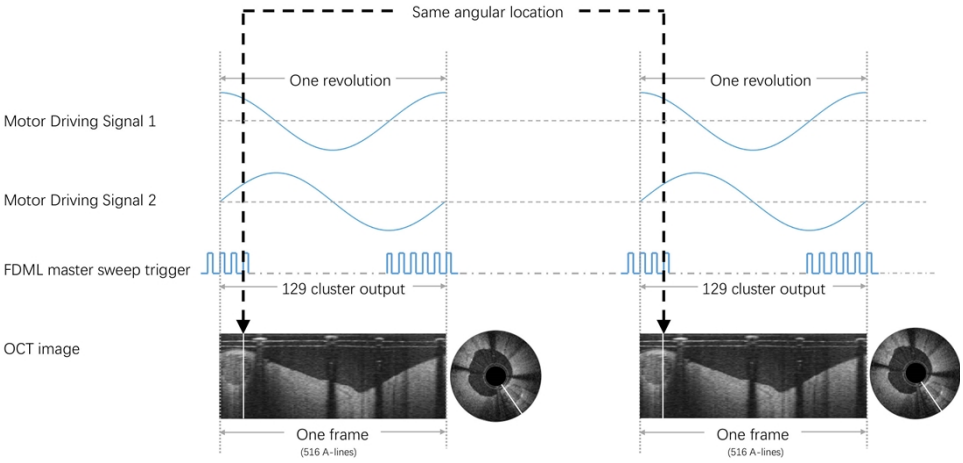

Fig. 3. Schematic diagram of synchronization between the motor drive signal, the FDML sweep output, data acquisition, and image reconstruction. The white lines indicate two co-registered and overlapping A-lines.

frame ($f + \Delta f$) according to [26,31,44]:

$$d(j,i,f) = \frac{\lambda}{4n_{ref}\pi}\,\Delta\varphi(j,i,f) = \frac{\lambda}{4n_{ref}\pi}tan^{-1}\left\{\frac{Im[I(j,\ i,f)I^*(j,i,f+\Delta f)]}{Re[I(j,\ i,f)I^*(j,i,f+\Delta f)]}\right\} \tag{1}$$

where Δf indicates the frame interval for the phase comparison, n_{ref} is the refractive index of the sample, I is the original complex OCT data, and λ is the centre wavelength of the FDML laser, which is 1316 nm in our case. The asterisk (*) denotes the complex conjugate. The radial strain ε is the displacement gradient along the radial direction, and was calculated by the central difference method with a window size of $2 \cdot \Delta j$:

$$\varepsilon(j,i,f) = \frac{d(j-\Delta j,i,f) - d(j+\Delta j,i,f)}{2\cdot\Delta j\cdot\Delta z} \tag{2}$$

where Δz is the spatial sample interval. Substitution of Eq. (1) yields

$$\varepsilon(j,i,f) = \frac{\lambda}{8\pi\cdot n_{ref}\cdot\Delta j\cdot\Delta z}(\Delta\varphi(j-\Delta j,i,f) - \Delta\varphi(j+\Delta j,i,f)) \tag{3}$$

In this formulation, compressive strain is positive. The measured phase shift $\Delta\varphi$ is affected by three factors: phase wrapping when the true phase shift is $>\pi$ or $<-\pi$, global phase offset $\Delta\varphi_g$ due to the displacement between the catheter and the sample, and the OCT phase noise. Taking these three factors into account, the experimentally measured phase shift $\Delta\varphi$ can be written as

$$\Delta\varphi\ (j,i,f) = \Delta\varphi_{dis}\ (j,i,f) + \sigma(j,i,f) + \Delta\varphi_g(i,f) + 2m(j,i,f)\pi \tag{4}$$

where $\Delta\varphi_{dis}$ is the true value induced by tissue displacement, σ is the OCT phase noise, and the last term indicates the phase wrapping. m is an integer and its value is unknown without applying phase unwrapping.

The global phase shift is cancelled out when calculating strain, since it does not change with radial depth. Phase wrapping can be avoided in Eq. (4) by choosing small enough pressure intervals. When this condition is fulfilled, only the phase noise affects the measurement. In our study, the data set was acquired at a rate of 3019 frames/s and the pressure difference between

Biomedical Optics EXPRESS

two neighbouring frames is small (< 0.06 mmHg, as determined from the maximum slope of the measured pressure), which allows us to choose a proper frame interval to avoid phase wrapping, while maintaining sufficient image contrast. The OCT phase noise σ is known to be associated with laser spectrum variance, data acquisition jitter, and fluctuation of the reference arm length [26,27]. Rather than measuring the contribution of each factor, we measured the overall phase noise σ to be 9.7 mrad, corresponding to 0.76 nm in tissue (with a 20-frame interval and 20-frame average). This number determines the minimum detectable displacement. The characterization of the phase stability and further suppression of the phase noise are detailed in Supplement 1.

The strain computed using Eq. (3) in 516 circumferential A-lines is transformed to a Cartesian grid by bilinear interpolation of the polar domain $\varepsilon(r, \theta)$ data to $\varepsilon\left(\sqrt{x^2 + y^2}, \tan^{-1}\left[\frac{y}{x}\right]\right)$ for each (x, y) coordinate pair.

2.5. Human samples and histology preparation

The human arteries were obtained from the Department of Pathology of the Erasmus University Medical Centre, in accordance with a protocol sanctioned by the local ethics committee (Institutional Review Board: Erasmus University Medical Centre, MEC-2019-0217). The arteries were obtained from two donors (LAD1: female, age: 58 and LAD2: male, age: 61) with non-cardiovascular cause of death. The arteries were dissected from the myocardial tissue within 24 hours post-mortem and snap-frozen. Then they were stored at -80° until the day of the experiments. Before the tests, they were thawed for 30 min at room temperature. The temperature of the water bath was maintained at 36.8°C during imaging. Following imaging, arteries were embedded in gelatin (VWR, The Netherlands) and frozen in preparation for cryosectioning. Cryosections were cut at 8 µm thickness. Sections were fixed in buffered formaldehyde (Boom BV, The Netherlands) and then stained using Resorcin-Fuchsin (RF) (basic fuchsin and ferri(III)chloride: Sigma Aldrich, The Netherlands; Resorcin: Merck, The Netherlands; 96% ethanol: Boom BV, The Netherlands; 37% HCl: Honeywell, The Netherlands) for elastin and collagen, and Oil-red-O (ORO) (Sigma-Aldrich, The Netherlands; 2-propanol: Honeywell, The Netherlands) for lipids.

3. Results

3.1. Imaging of stable phantom

IV-OCE imaging experiments were first carried out in the PVA phantom while maintaining a constant intraluminal pressure. Figures 4(a)-(c) shows the conventional OCT images that were reconstructed using the absolute value of the complex OCT data set. Four shadow areas can be seen in the image, which were induced by the wires of the micromotor. The boundary of the inclusion is visible in the OCT image, and the image appearance inside the inclusion is similar to that of the PVA phantom. We acquired 200 frames using the motorized catheter and displayed them on the right panel in **Visualization 2** at 20 frames/s playback speed; motion cannot be detected visually.

To demonstrate the imaging stability, we applied frame averaging over 20 and 100 frames and then assessed image sharpness, since any scan speed variation will blur the image when applying frame averaging [45–47]. Figures 4(a)-(c) show the intensity images before and after frame averaging at the same dynamic range. Sharpness was preserved, even after applying frame averaging over 100 frames, while the noise was reduced. Figures 4(d)-(f) magnify a bright feature of the phantom (indicated by dashed boxes), demonstrating stability down to sample scale (also shown on the right panel in **Visualization 2**). Figure 4(g) shows the intensity plot of one axial line (A-line) before and after frame averaging, demonstrating preserved features (indicated by the dashed arrows) and reduced noise. Since 20-frame averaging achieved similar noise suppression to 100-frame averaging, we chose 20-frame averaging to improve the image quality for all conventional OCT images.

Biomedical Optics EXPRESS

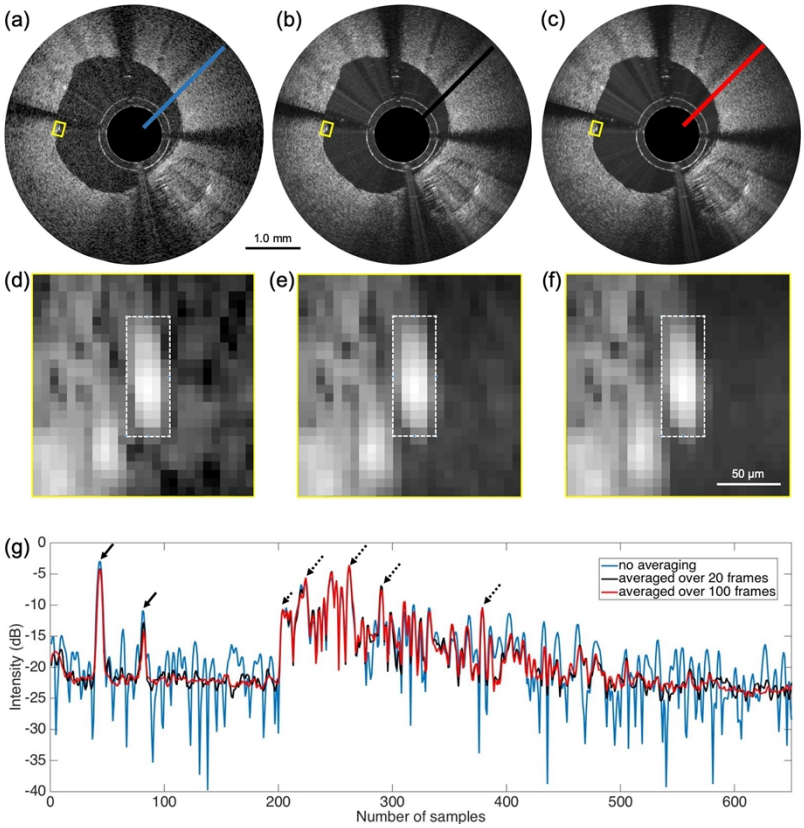

Fig. 4. (a-c) OCT images of the PVA phantom (a) without frame averaging, (b) with 20-frame averaging, and (c) with 100-frame averaging. (d-f) Magnification of a bright feature of the phantom to pixel level, as highlighted by the dashed boxes in (d-f) and indicated by the yellow boxes in (a-c). (g) Amplitude plots of one axial line (A-line) data as indicated by blue, black and red lines in (a-c). The solid arrows indicate the catheter tube, and the dashed arrows indicate speckle maxima in the OCT signal.

The importance of scan stability on the displacement image can be seen by a calculation of the phase difference between two aligned frames, compared to intentionally mismatched frames (±1 A-line, 0.7° angular). The interval between two aligned frames was 20 frames (~ 6.7 ms interval). As shown in Fig. 5(b) and (d), the small artificial mismatch washes out the phase shift signal that could be reliably extracted in Fig. 5(c). In absence of an intraluminal pressure change, no strain was induced, and the stiff inclusion cannot be distinguished from the surrounding soft phantom material. The measured phase shift here is almost uniform, indicating it is caused by the relative displacement between the catheter and the phantom. This global motion (of approximately 0 - 50 nm) is not noticeable in the intensity image but can clearly be seen in the phase shift, which is highly sensitive to displacements at sub-sample scale. A video was recorded showing both the structural image and phase-shift image (**Visualization 3**).

3.2. Dynamic strain imaging in a phantom

We introduced a dynamic intraluminal pressure to visualize the strain effected in the phantom. For 300 ms after starting the recording, the pressure was maintained at 84 mmHg by applying a constant infusion rate. Upon stopping the infusion, the pressure dropped to approximately

Biomedical Optics EXPRESS

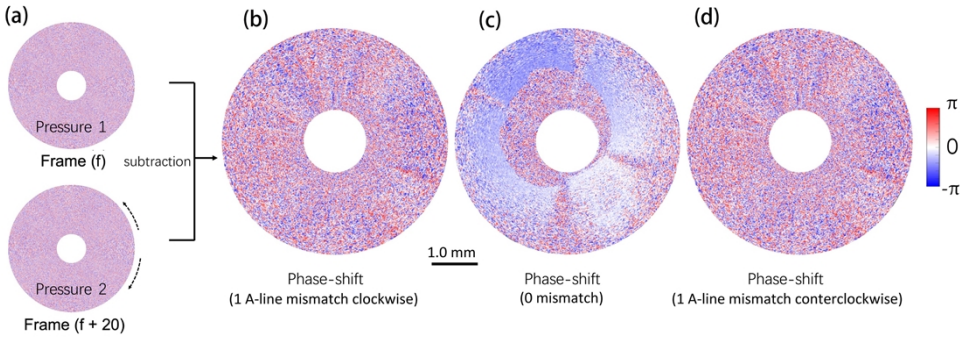

Fig. 5. (a) OCT signal phase in two frames at constant pressure, (f) and (f+20). Frame (f+20) was shifted by one A-line clockwise in (b), zero A-lines in (c), and one A-line counterclockwise in (d). Only without mismatch in (c) could the phase shift be successfully extracted.

24 mmHg over 700 ms; a pressure difference and rate of change that is comparable to the physiological variation in the normal cardiac cycle [48]. The deformation of the phantom during this sequence was imaged by IV-OCE. We first analysed the phase shift during the pressure drop using frame intervals of 1, 10, 20, and 50 frames (corresponding to pressure drops of 0.06, 0.48, 1.0, and 2.31 mmHg as measured by the transducer). As shown in Fig. 6(a)-(d), the phase shift changes gradually along the radial depth due to the radial strain induced by the pressure change. Phase wrapping (π to -π jumps) along the radial direction, can be seen in the soft PVA phantom but not in the VWP inclusion due to its high stiffness.

Figure 6(e)-(h) shows the strain images that correspond to Fig. 6(a)-(d). The radial strain was calculated as the gradient of the displacement over a radial depth range of 20 samples (~74 μm in n_{ref} = 1.34), using a central finite difference approximation. It can be seen that the strain in the PVA phantom increases with the pressure difference, while the strain in the VWP inclusion remains close to zero. This image contrast distinguishes the stiff inclusion from the soft PVA phantom.

A larger pressure difference (and thus frame interval) produces a proportionally larger strain and thus greater contrast. Phase wrapping can be avoided if a small enough frame interval is chosen. Figure 6(i) plots the phase shift at two points on one A-line with 20-sample difference in radial depth, and Fig. 6(j) plots the phase shift gradient on the 20-sample window as a function of frame interval. This experiment demonstrates that no wrapping of the phase shift gradient occurs for a frame interval < 27 frames, in this moderately stiff homogeneous phantom. Therefore, for the subsequent experiments, we chose an interval of 20 frames to extract the phase shift, calculate the gradient, and reconstruct the strain images. The interval and window may be chosen shorter for softer materials which exhibit larger displacement and strain.

Figure 7 shows dynamic strain imaging in the phantom. At constant pressure, only the phase shift induced by the global displacement between the catheter and the phantom can be detected (Fig. 7(d)). The strain is zero everywhere as shown in Fig. 7(g). In the presence of a pressure differential, the inclusion shows a much lower strain than the surrounding soft phantom in Fig. 7(h). Due to the highly overlapping frames, frame averaging could be applied over 20 subsequent strain images to suppress the phase noise and improve the image contrast, as shown in Fig. 7(k). Figure 7(c),(f),i,l show the IV-OCE images acquired over a smaller pressure drop, resulting in a smaller strain in Fig. 7(l), compared to Fig. 7(k). An FEM simulation was also performed, which shows results similar to our strain image. The details of the simulation can be found in Supplement 1. In the structural OCT images (Fig. 7(a)-(c)), no tissue deformation can

Biomedical Optics EXPRESS

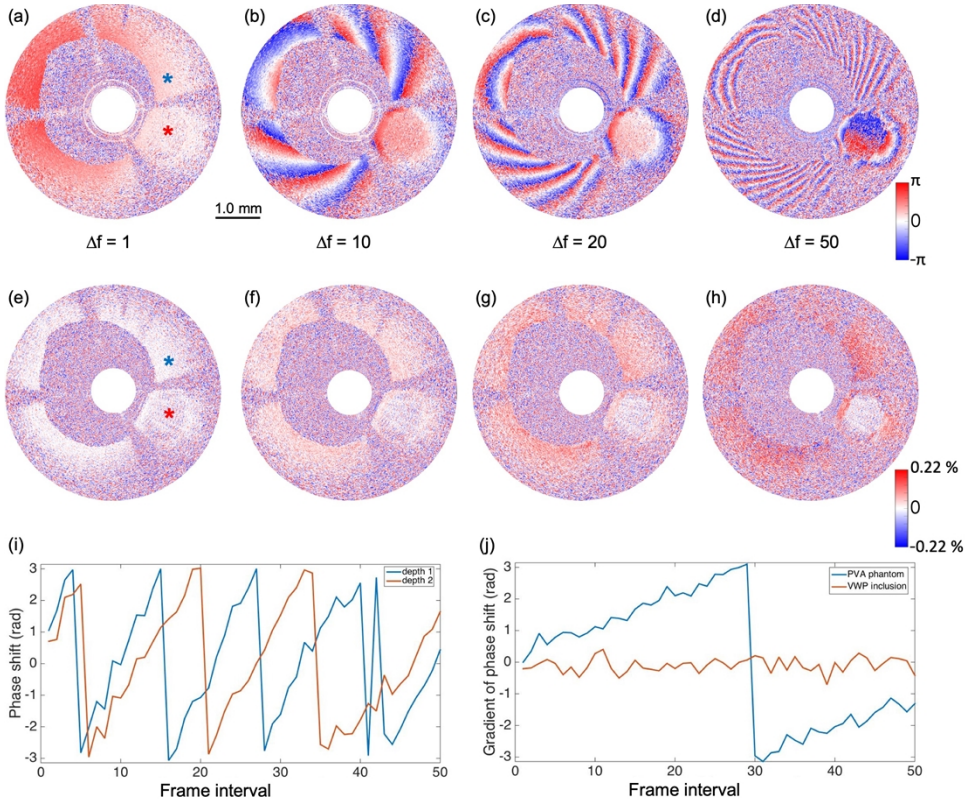

Fig. 6. Phase shift and gradient of phase shift calculated over 20 pixels along the radial depth. (a-d) Phase shift between two frames with a frame interval of (a) 1 frame, (b) 10 frames, (c) 20 frames, and (d) 50 frames. (e-h) Gradient of phase shift over 20 samples calculated with a frame interval of (e) 1 frame, (f) 10 frames, (g) 20 frames, and (h) 50 frames. (i) Phase shift as a function of frame interval of two samples with 20-sample difference in radial depth (blue asterisk in a). (j) Gradient of phase shift calculated based on the two pixels in (i), which changes with frame interval in VWP (red line and red asterisk) and PVA phantom (blue line and blue asterisk). Δf indicates the frame interval.

Biomedical Optics EXPRESS

be seen, and the only noticeable change was the lumen size of the phantom. A video was made to show the dynamic strain imaging at 150 frames/s playback speed in **Visualization 4**.

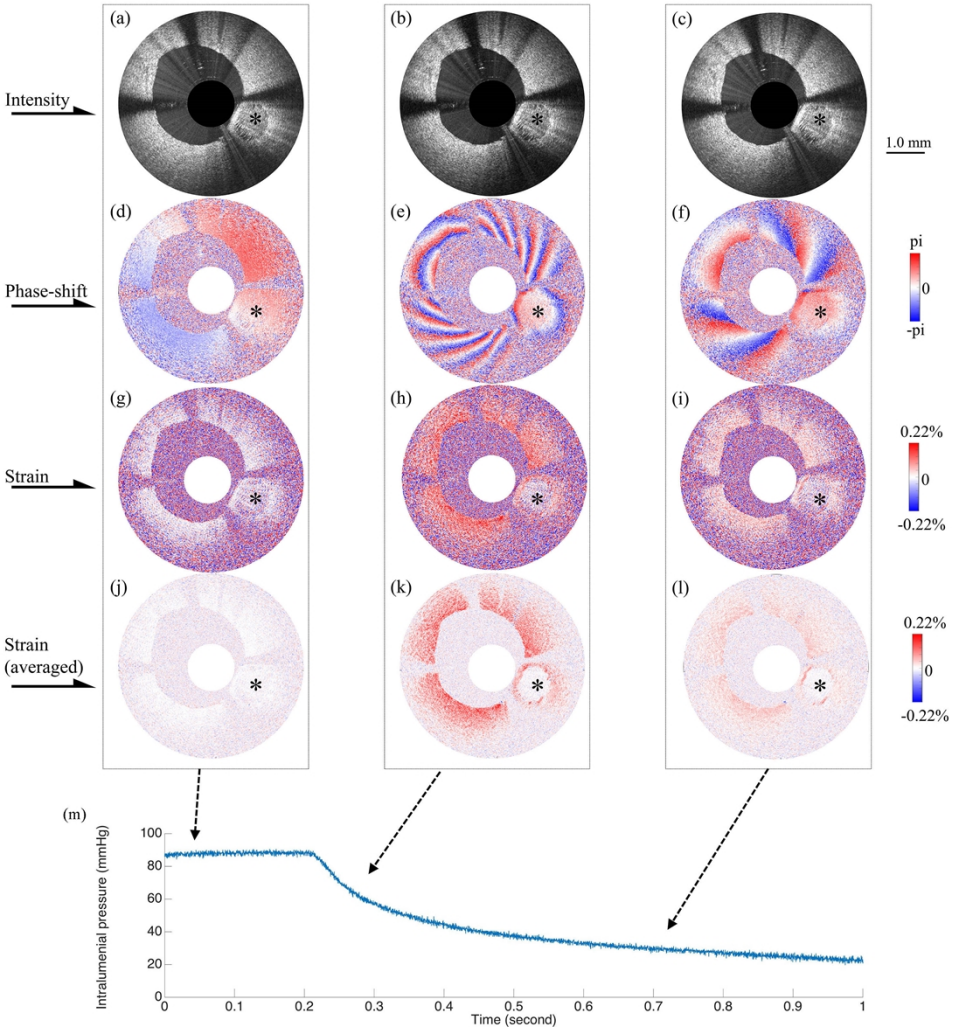

Fig. 7. Dynamic IV-OCE imaging of PVA phantom and VWP inclusion. (a-c) Intensity OCT images, (d-f) corresponding phase shift images, (g-i) strain images, and (j-l) strain images after 20-frame averaging. (m) Plot of measured intraluminal pressure over time. Asterisks indicate the area of the stiff VWP inclusion. (a,d,g,j) were acquired at constant pressure (zero strain). (b,e,h,k) were acquired during rapid pressure change (large strain). (c,f,i,l) were acquired during slow pressure change (small strain).

3.3. Ex vivo strain imaging of calcified and collagenous atherosclerotic plaques

Ex vivo strain images were acquired in two human left anterior descending (LAD) arteries, respectively. The experimental set-up and image processing were the same as in the phantom study, except the temperature of the experiment was maintained at 36.8°C.

The conventional OCT image features in LAD2 suggest the possible existence of two calcifications (yellow asterisks) because of the clear boundary of the calcified area as shown in Fig. 8(d) [49]. Similarly, abnormal tissue (black asterisk) can be found in LAD1 as shown

Biomedical Optics EXPRESS

in Fig. 8(a). However, it is difficult to identify the plaque type based on the structural image appearance alone. The IV-OCE images (as shown in Fig. 8(b),(e)) show the strain in the plaques. It can be seen in Fig. 8(e) that the calcified plaques exhibit a low strain value, which has been reported by IVUS elastography previously [21]. This low strain reflects the high stiffness of calcifications. Low strain can also be seen in the plaque in Fig. 8(b), suggesting a possible existence of a relatively stiff tissue type, consistent with collagen. Using histology as a gold standard, the presence of calcified plaque and collagen-rich plaque was confirmed. A collagen-rich fibrous area can be seen near the surface in Fig. 8(c) (red area, black asterisk) and calcifications can be seen in the Fig. 8(f) (dark blue calcium borders, yellow asterisk). The healthy arterial wall (Fig. 8(a),(b),(c), 3 o'clock to 9 o'clock) exhibits moderate strain, while two high strain spots appear at the transition regions to collagen-rich plaque, indicated by blue arrows in Fig. 8(b). The transition regions, also referred to as shoulder regions, demonstrate higher strains and stresses due to the increased local curvature in the lumen as shown previously [50].

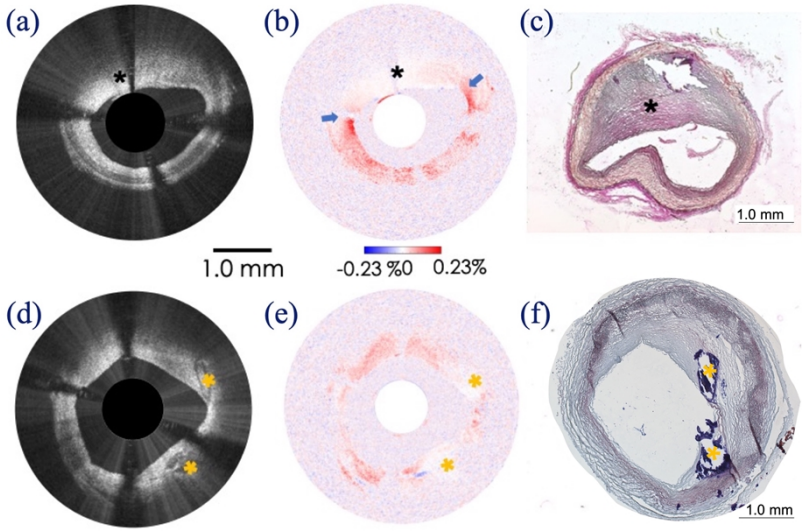

Fig. 8. *Ex vivo* IV-OCE images acquired in two human LAD arteries: (a-c) were acquired in LAD1 while (d-f) were acquired independently in LAD2. (a, d) Structural OCT images show the typical morphology of collagen-rich plaque in (a) and plaque with calcified inclusions in (d). (b,e) Strain images show the low strain of the plaque and inclusions. (c,f) Histology shows an atherosclerotic plaque with a collagen-rich fibrous area near the surface (c, resorcin-fuchsin [RF] stain, collagen in red, black asterisk) and a plaque with calcifications (f, Oil Red O [ORO]/hematoxylin stain, calcification with dark blue boundary and mineralized appearance, yellow asterisks).

4. Discussion and conclusion

In this study, we demonstrate the first IV-OCE using an intravascular motorized catheter, a megahertz FDML OCT system, and a proximal flushing pump. The stable beam scanning offered by the catheter and careful synchronization allow us to resolve the phase shift between two frames sample by sample. Using the proximal flushing pump, an intraluminal pressure change was induced. Phase wrapping was prevented in the strain calculation by choosing a small frame interval. At an imaging speed of 3019 frames/s, IV-OCE can capture the dynamic strain induced by the pressure change. Combining these advances in system control, catheter engineering, signal processing and image analysis, strain images and structural OCT images are simultaneously

Biomedical Optics EXPRESS

provided by a catheter-based imaging system. In the strain images, a stiff inclusion implanted in a soft phantom can be easily distinguished. Similarly, stiff calcified and collagen-rich plaques can be identified by IV-OCE.

Several approaches have been demonstrated towards endoscopic realization of OCE [30,51–53]. One common approach is to turn off the beam scanning of the catheter while measuring strain (as M-mode imaging). In this way, tissue deformation is only measured at a single angular or transverse location rather than over the entire circumferential cross-section [51–53]. Another approach induces rapid tissue displacement using the acoustic radiation force (ARF) generated by an ultrasound transducer [54]. The rapid displacement induced by the ARF can be resolved between two adjacent A-lines, and a cross-sectional endoscopic OCE image can be achieved using slow beam scanning. However, the ARF stimulus normally requires a transducer that is too large to integrate into a catheter that is compatible with intravascular imaging [30]. Anatomic OCT accesses tissue stiffness by tracking the lumen change, and has been applied in airway imaging [55]. Anatomic OCT processes the OCT intensity images rather than the phase signal. Localized tissue compliance can be extracted [56], but not actual tissue strain, which requires the imaging of displacement in the tissue with nanometre accuracy.

In our study, the radial strain was calculated as the phase shift gradient over an appropriate radial depth. To calculate the phase shift gradient, we used a linear symmetric finite difference method, a straightforward method that has low computational cost [31,57]. The strain calculation may be refined using advanced methods, such as intensity-weighted ordinary least squares [31,58]. Besides the phase processing method, a speckle-based or complex-decorrelation-based analysis can also be used for signal processing [24,59], which may yield the measured strain deformation not only along the radial direction but also along the transverse direction [60]. Applying such a method to IV-OCE data, circumferential strain may potentially yield a 2D strain measurement, from which the principal strain can be computed.

We qualitatively interpreted features of the strain image in terms tissue stiffness. Because the deformation is small and the lumen of the sample is close to round, we consider the stress distribution to be symmetric, i.e., the stress is similar at the same radial depth. However, the heterogeneity, anisotropy, and presence of plaques or vessel bifurcations may lead to non-symmetric geometries, thus affecting the stress distribution and interpretation of strain as stiffness [61,62]. The measured strain depends on the catheter position relative to the lumen center [63]. Future quantitative studies will combine structural images and strain images with computational models to yield quantitative tissue elasticity maps [64,65]. Arterial tissues exhibit Young's moduli that range over three orders of magnitude (kPa to MPa), and are very challenging to quantify exactly [61]. Strain-based elastography methods have a limited dynamic range. In vascular imaging, the contrast between soft (lipid-rich), stiffer (fibrous) and hard (calcium) tissues is relevant. The method has been tuned to be sensitive to strain in softer materials. Although the Young's modulus of the inclusion in these experiments is outside of the range of vascular tissue constituents, the measured strain patterns in the softer material will not be affected by the exact stiffness of the hard inclusion.

In the clinical practice of IV-OCT, radiocontrast dye or saline is used to flush away the highly scattering red blood cells at a rate of 3-5 ml/s [6]. The mechanical actuation method we applied in this study can potentially be achieved by modifying the clinical flushing procedure. Our data demonstrate that a pressure change of 1.0 mmHg already induces sufficient imaging contrast for IV-OCE (Fig. 4(g)). The images were acquired at a base pressure of around 80 mmHg, which is within the normal coronary artery pressure range (60–140 mmHg) [66]. Therefore, beyond a modulated flushing, the coronary artery pressure change itself could also be sufficient for inducing a measurable strain for IV-OCE. Future *in vivo* experiments in animal models will inform optimization of the excitation method. Volumetric IV-OCE imaging of an entire coronary

Biomedical Optics EXPRESS

artery could potentially be achieved using a step-by-step pullback, sampling OCE images acquired in a manner similar to the *in vitro* results described here, at 500 μm to 1 mm intervals.

Several parameters, such as the frame interval, window size of the strain calculation, and the number of frames used for averaging, may be tuned to optimize the *in vivo* imaging quality. The OCT intensity data could be applied for masking out areas with low signal in the strain image. In principle, it is possible to achieve IV-OCE at a conventional frame rate of approximately 150 frames/s. However, at this lower speed, the motorized catheter scan stability is insufficient for reliably computing frame-based phase differences, nor is the noise reduction by frame averaging feasible. We expect the laser's phase stability and imaging speed to be compatible with *in vivo* imaging. The 1.1 mm diameter motorized catheter can also be used for an *in vivo* imaging study as demonstrated previously [32].

In PCI procedures, heavily calcified stenoses require aggressive lesion preparation, mainly owing to the large stiffness of calcification. Methods to image and quantify the calcification, such as IV-OCE, are of immediate interest to clinical users of IV-OCT. In our study, not only the calcified plaque but also the collagenous area is found to be stiff by IV-OCE, which may serve to distinguish it from lipid-rich plaque that can sometimes have a similar OCT appearance. Our set of coronary artery samples did not include lipid-rich plaques (the collection was complicated by the COVID-19 pandemic). Future extension and diversification of our sample set will not only deepen our understanding of the formation of atherosclerotic plaque but also unlock this information for diagnostic use. In particular, biomechanical simulation studies predict a high stress/strain area near the shoulder of plaques, which has never been clearly demonstrated experimentally to date [50,67,68]. Figure 8(b) demonstrates these high strain spots in a pattern consistent with those observed in simulations [50,59,67]. IVUS-based elastography has focused on high-strain signatures of lipid-rich plaques, which have been implicated in the elevated risk of ischaemic events [22]. However, its imaging resolution and strain sensitivity are inferior by a factor of approximately 10 compared to IV-OCE [69]. In the future, we believe IV-OCE will become a powerful tool for investigating the mechanism of plaque rupture. Combining the morphological OCT image, mechanical OCE image, and biomechanical FEM simulation may possibly offer a comprehensive risk assessment for plaque vulnerability and associated acute coronary syndrome.

Beyond cardiovascular applications, it is possible to acquire strain images in other luminal organs, such as the airways and the gastrointestinal tract, where passive stimuli (tidal breath and gastrointestinal motility) may induce sufficient tissue stress to offer a detectable strain [55,56]. Abnormal tissue types, such as tumour and lung fibrosis, are usually associated with different stiffnesses compared with the surrounding healthy tissue [69,70], and the diagnosis normally requires tissue removal for biopsy assessment. Visualizing the strain and the morphology at the same time *in vivo* will certainly bring new opportunities to the study, diagnosis, and treatment of these diseases while avoiding tissue removal from patients.

Funding. Nederlandse Organisatie voor Wetenschappelijk Onderzoek (15940); ZonMw (104003006); Bundesministerium für Bildung und Forschung (13GW0227B); Deutsche Forschungsgemeinschaft (EXC 2167-390884018, HU1006/6 270871130); State of Schleswig-Holstein (Excellence Chair Program).

Acknowledgement. The authors acknowledge Geert Springeling for his contribution to the catheter assembly and phantom preparation. The authors acknowledge Antonio Lopez Marin for his contribution to the beam characterization. The authors acknowledge Maaike te Lintel Hekkert and Liesbeth Eekhout for their contributions to the pressure measurement. The authors acknowledge Wolfgang Wieser for his contribution to the FDML operation. T. Wang acknowledges Dr. Brendan F. Kennedy for the fruitful discussion on the axial strain processing. T. Wang acknowledges the late Dr. Charles Lancee for inventing the dual-layer coil and for his supervision of micro-engine development.

Disclosures. Robert Huber has financial interest in Optores Gmbh that commercializes FDML technology. The other authors declare no relationship with industry in the context of this work.

Data Availability. Data underlying the results presented in this paper are not publicly available at this time but may be obtained from the corresponding authors upon request.

Biomedical Optics EXPRESS

Supplemental document. See Supplement 1 for supporting content.

References

1. D. Huang, E. A. Swanson, C. P. Lin, J. S. Schuman, W. G. Stinson, W. Chang, M. R. Hee, T. Flotte, K. Gregory, C. A. Puliafito, and J. G. Fujimoto, "Optical coherence tomography," Science **254**(5035), 1178–1181 (1991).
2. M. R. Hee, J. A. Izatt, E. A. Swanson, D. Huang, J. S. Schuman, C. P. Lin, C. A. Puliafito, and J. G. Fujimoto, "Optical coherence tomography of the human retina," Arch. Ophthalmol. **113**(3), 325–332 (1995).
3. G. J. Tearney, M. E. Brezinski, B. E. Bouma, S. A. Boppart, C. Pitris, J. F. Southern, and J. G. Fujimoto, "In vivo endoscopic optical biopsy with optical coherence tomography," Science **276**(5321), 2037–2039 (1997).
4. W. Drexler and J. G. Fujimoto, *Optical Coherence Tomography: Technology and Applications* (Springer, 2015).
5. M. J. Gora, M. J. Suter, G. J. Tearney, and X. Li, "Endoscopic optical coherence tomography: technologies and clinical applications [Invited]," Biomed. Opt. Express **8**(5), 2405–2444 (2017).
6. G. J. Tearney, E. Regar, and T. Akasaka, *et al.*, "Consensus standards for acquisition, measurement, and reporting of intravascular optical coherence tomography studies: a report from the International Working Group for Intravascular Optical Coherence Tomography Standardization and Validation," J. Am. Coll. Cardiol. **59**(12), 1058–1072 (2012).
7. B. E. Bouma, M. Villiger, K. Otsuka, and W. Y. Oh, "Intravascular optical coherence tomography [Invited]," Biomed. Opt. Express **8**(5), 2660–2686 (2017).
8. I. K. Jang, G. Tearney, and B. Bouma, "Visualization of tissue prolapse between coronary stent struts by optical coherence tomography: comparison with intravascular ultrasound," Circulation **104**(22), 2754 (2001).
9. E. A. Swanson and J. G. Fujimoto, "The ecosystem that powered the translation of OCT from fundamental research to clinical and commercial impact [Invited]," Biomed. Opt. Express **8**(3), 1638–1664 (2017).
10. T. W. Johnson, L. Raber, and C. di Mario, *et al.*, "Clinical use of intracoronary imaging. Part 2: acute coronary syndromes, ambiguous coronary angiography findings, and guiding interventional decision-making: an expert consensus document of the European Association of Percutaneous Cardiovascular Interventions," Eur. Heart J. **40**(31), 2566–2584 (2019).
11. Z. A. Ali, A. Maehara, P. Genereux, R. A. Shlofmitz, F. Fabbiocchi, T. M. Nazif, G. Guagliumi, P. M. Meraj, F. Alfonso, H. Samady, T. Akasaka, E. B. Carlson, M. A. Leesar, M. Matsumura, M. O. Ozan, G. S. Mintz, O. Ben-Yehuda, G. W. Stone, and I. I. O. P. Investigators, "Optical coherence tomography compared with intravascular ultrasound and with angiography to guide coronary stent implantation (ILUMIEN III: OPTIMIZE PCI): a randomised controlled trial," Lancet **388**(10060), 2618–2628 (2016).
12. K. Karimi Galougahi, E. Shlofmitz, A. Jeremias, S. Gogia, A. J. Kirtane, J. M. Hill, D. Karmpaliotis, G. S. Mintz, A. Maehara, G. W. Stone, R. A. Shlofmitz, and Z. A. Ali, "Therapeutic approach to calcified coronary lesions: disruptive technologies," Curr. Cardiol. Rep. **23**(4), 33 (2021).
13. G. van Soest, E. Regar, T. P. Goderie, N. Gonzalo, S. Koljenovic, G. J. van Leenders, P. W. Serruys, and A. F. van der Steen, "Pitfalls in plaque characterization by OCT: image artifacts in native coronary arteries," JACC Cardiovasc Imaging **4**(7), 810–813 (2011).
14. O. Manfrini, E. Mont, O. Leone, E. Arbustini, V. Eusebi, R. Virmani, and R. Bugiardini, "Sources of error and interpretation of plaque morphology by optical coherence tomography," Am. J. Cardiol. **98**(2), 156–159 (2006).
15. G. J. Ughi, H. Wang, E. Gerbaud, J. A. Gardecki, A. M. Fard, E. Hamidi, P. Vacas-Jacques, M. Rosenberg, F. A. Jaffer, and G. J. Tearney, "Clinical characterization of coronary atherosclerosis with dual-modality OCT and near-infrared autofluorescence imaging," JACC Cardiovasc Imaging **9**(11), 1304–1314 (2016).
16. C. V. Bourantas, F. A. Jaffer, F. J. Gijsen, G. van Soest, S. P. Madden, B. K. Courtney, A. M. Fard, E. Tenekecioglu, Y. Zeng, A. F. W. van der Steen, S. Emelianov, J. Muller, P. H. Stone, L. Marcu, G. J. Tearney, and P. W. Serruys, "Hybrid intravascular imaging: recent advances, technical considerations, and current applications in the study of plaque pathophysiology," Eur. Heart J. **38**(6), 400–412 (2017).
17. A. M. Fard, P. Vacas-Jacques, E. Hamidi, H. Wang, R. W. Carruth, J. A. Gardecki, and G. J. Tearney, "Optical coherence tomography–near infrared spectroscopy system and catheter for intravascular imaging," Opt. Express **21**(25), 30849–30858 (2013).
18. G. van Soest, T. Goderie, E. Regar, S. Koljenovic, G. L. van Leenders, N. Gonzalo, S. van Noorden, T. Okamura, B. E. Bouma, G. J. Tearney, J. W. Oosterhuis, P. W. Serruys, and A. F. van der Steen, "Atherosclerotic tissue characterization in vivo by optical coherence tomography attenuation imaging," J. Biomed. Opt. **15**(1), 011105 (2010).
19. J. N. van der Sijde, A. Karanasos, M. Villiger, B. E. Bouma, and E. Regar, "First-in-man assessment of plaque rupture by polarization-sensitive optical frequency domain imaging in vivo," Eur. Heart J. **37**(24), 1932 (2016).
20. H. S. Nam, J. W. Song, S. J. Jang, J. J. Lee, W. Y. Oh, J. W. Kim, and H. Yoo, "Characterization of lipid-rich plaques using spectroscopic optical coherence tomography," J. Biomed. Opt. **21**(7), 075004 (2016).
21. C. L. de Korte, A. F. W. van der Steen, E. I. Cespedes, G. Pasterkamp, S. G. Carlier, F. Mastik, A. H. Schoneveld, P. W. Serruys, and N. Bom, "Characterization of plaque components and vulnerability with intravascular ultrasound elastography," Phys. Med. Biol. **45**(6), 1465–1475 (2000).
22. J. A. Schaar, C. L. de Korte, F. Mastik, C. Strijder, G. Pasterkamp, E. Boersma, P. W. Serruys, and A. F. W. van der Steen, "Characterizing vulnerable plaque features with intravascular elastography," Circulation **108**(21), 2636–2641 (2003).

Biomedical Optics EXPRESS

23. J. A. Schaar, E. Regar, F. Mastik, E. P. McFadden, F. Saia, C. Disco, C. L. de Korte, P. J. de Feyter, A. F. W. van der Steen, and P. W. Serruys, "Incidence of high-strain patterns in human coronary arteries - Assessment with three-dimensional intravascular palpography and correlation with clinical presentation," Circulation **109**(22), 2716–2719 (2004).
24. X. Liang, V. Crecea, and S. A. Boppart, "Dynamic Optical Coherence Elastography: A Review," J. Innov. Opt. Health. Sci. **03**(04), 221–233 (2010).
25. S. Wang and K. V. Larin, "Optical coherence elastography for tissue characterization: a review," J. Biophotonics **8**(4), 279–302 (2015).
26. K. V. Larin and D. D. Sampson, "Optical coherence elastography - OCT at work in tissue biomechanics [Invited]," Biomed. Opt. Express **8**(2), 1172–1202 (2017).
27. B. F. Kennedy, X. Liang, S. G. Adie, D. K. Gerstmann, B. C. Quirk, S. A. Boppart, and D. D. Sampson, "In vivo three-dimensional optical coherence elastography," Opt. Express **19**(7), 6623–6634 (2011).
28. C. L. de Korte, S. G. Carlier, F. Mastik, M. M. Doyley, A. F. W. van der Steen, P. W. Serruys, and N. Bom, "Morphological and mechanical information of coronary arteries obtained with intravascular elastography. Feasibility study in vivo," Eur. Heart J. **23**(5), 405–413 (2002).
29. C. L. de Korte, M. J. Sierevogel, F. Mastik, C. Strijder, J. A. Schaar, E. Velema, G. Pasterkamp, P. W. Serruys, and A. F. W. van der Steen, "Identification of atherosclerotic plaque components with intravascular ultrasound elastography in vivo A Yucatan pig study," Circulation **105**(14), 1627–1630 (2002).
30. Y. Qu, T. Ma, Y. He, M. Yu, J. Zhu, Y. Miao, C. Dai, P. Patel, K. K. Shung, Q. Zhou, and Z. Chen, "Miniature probe for mapping mechanical properties of vascular lesions using acoustic radiation force optical coherence elastography," Sci. Rep. **7**(1), 4731 (2017).
31. B. F. Kennedy, S. H. Koh, R. A. McLaughlin, K. M. Kennedy, P. R. Munro, and D. D. Sampson, "Strain estimation in phase-sensitive optical coherence elastography," Biomed. Opt. Express **3**(8), 1865–1879 (2012).
32. T. Wang, T. Pfeiffer, E. Regar, W. Wieser, H. van Beusekom, C. T. Lancee, G. Springeling, I. Krabbendam, A. F. van der Steen, R. Huber, and G. van Soest, "Heartbeat OCT: in vivo intravascular megahertz-optical coherence tomography," Biomed. Opt. Express **6**(12), 5021–5032 (2015).
33. T. H. Tsai, B. Potsaid, Y. K. Tao, V. Jayaraman, J. Jiang, P. J. Heim, M. F. Kraus, C. Zhou, J. Hornegger, H. Mashimo, A. E. Cable, and J. G. Fujimoto, "Ultrahigh speed endoscopic optical coherence tomography using micromotor imaging catheter and VCSEL technology," Biomed. Opt. Express **4**(7), 1119–1132 (2013).
34. J. Mavadia-Shukla, P. Fathi, W. Liang, S. Wu, C. Sears, and X. Li, "High-speed, ultrahigh-resolution distal scanning OCT endoscopy at 800 nm for in vivo imaging of colon tumorigenesis on murine models," Biomed. Opt. Express **9**(8), 3731–3739 (2018).
35. A. Lopez-Marin, G. Springeling, R. Beurskens, H. van Beusekom, A. F. W. van der Steen, A. D. Koch, B. E. Bouma, R. Huber, G. van Soest, and T. Wang, "Motorized capsule for shadow-free OCT imaging and synchronous beam control," Opt. Lett. **44**(15), 3641–3644 (2019).
36. T. Wang, C. Lancée, R. Beurskens, J. Meijer, B. Knapen, A. F. W. van der Steen, and G. van Soest, "Development of a high-speed synchronous micro motor and its application in intravascular imaging," Sens. Actuators, A **218**, 60–68 (2014).
37. G. Lamouche, B. F. Kennedy, K. M. Kennedy, C.-E. Bisaillon, A. Curatolo, G. Campbell, V. Pazos, and D. D. Sampson, "Review of tissue simulating phantoms with controllable optical, mechanical and structural properties for use in optical coherence tomography," Biomed. Opt. Express **3**(6), 1381–1398 (2012).
38. J. Mueller, D. Courty, M. Spielhofer, R. Spolenak, and K. Shea, "Mechanical properties of interfaces in inkjet 3D printed single- and multi-material parts," 3D Printing and Additive Manufacturing **4**(4), 193–199 (2017).
39. R. Huber, M. Wojtkowski, and J. G. Fujimoto, "Fourier Domain Mode Locking (FDML): A new laser operating regime and applications for optical coherence tomography," Opt. Express **14**(8), 3225–3237 (2006).
40. W. Wieser, B. R. Biedermann, T. Klein, C. M. Eigenwillig, and R. Huber, "Multi-Megahertz OCT: High quality 3D imaging at 20 million A-scans and 4.5 GVoxels per second,"
41. T. Wang, T. Pfeiffer, M. Wu, W. Wieser, G. Amenta, W. Draxinger, A. F. W. van der Steen, R. Huber, and G. V. Soest, "Thermo-elastic optical coherence tomography," Opt. Lett. **42**(17), 3466–3469 (2017).
42. W. Wieser, T. Klein, W. Draxinger, and R. Huber, "Fully automated 1.5 MHz FDML laser with more than 100 mW output power at 1310 nm," Proc. SPIE **9541**, 954116 (2015).
43. T. Wang, T. Pfeiffer, J. Daemen, F. Mastik, W. Wieser, A. F. W. van der Steen, R. Huber, and G. van Soest, "Simultaneous Morphological and Flow Imaging Enabled by Megahertz Intravascular Doppler Optical Coherence Tomography," IEEE Trans. Med. Imaging **39**(5), 1535–1544 (2020).
44. R. K. Wang, Z. Ma, and S. J. Kirkpatrick, "Tissue Doppler optical coherence elastography for real time strain rate and strain mapping of soft tissue," Appl. Phys. Lett. **89**(14), 144103 (2006).
45. B. F. Kennedy, A. Curatolo, D. D. Sampson, T. R. Hillman, and C. Saunders, *Speckle reduction in optical coherence tomography images using tissue viscoelasticity* (SPIE, 2011).
46. K. Shen, H. Lu, S. Baig, and M. R. Wang, "Improving lateral resolution and image quality of optical coherence tomography by the multi-frame superresolution technique for 3D tissue imaging," Biomed. Opt. Express **8**(11), 4887–4918 (2017).
47. C. Cuartas-Velez, R. Restrepo, B. E. Bouma, and N. Uribe-Patarroyo, "Volumetric non-local-means based speckle reduction for optical coherence tomography," Biomed. Opt. Express **9**(7), 3354–3372 (2018).

Biomedical Optics EXPRESS

48. R. M. Berne, "Regulation of coronary blood flow," Physiol. Rev. **44**(1), 1–29 (1964).
49. H. Yabushita, B. E. Bouma, S. L. Houser, H. T. Aretz, I. K. Jang, K. H. Schlendorf, C. R. Kauffman, M. Shishkov, D. H. Kang, E. F. Halpern, and G. J. Tearney, "Characterization of human atherosclerosis by optical coherence tomography," Circulation **106**(13), 1640–1645 (2002).
50. A. C. Akyildiz, L. Speelman, H. A. Nieuwstadt, H. van Brummelen, R. Virmani, A. van der Lugt, A. F. van der Steen, J. J. Wentzel, and F. J. Gijsen, "The effects of plaque morphology and material properties on peak cap stress in human coronary arteries," Comput. Methods Biomech. Biomed. Eng. **19**(7), 771–779 (2016).
51. Y. Qiu, F. R. Zaki, N. Chandra, S. A. Chester, and X. Liu, "Nonlinear characterization of elasticity using quantitative optical coherence elastography," Biomed. Opt. Express **7**(11), 4702–4710 (2016).
52. X. Liu, F. R. Zaki, H. Wu, C. Wang, and Y. Wang, "Temporally and spatially adaptive Doppler analysis for robust handheld optical coherence elastography," Biomed. Opt. Express **9**(7), 3335–3353 (2018).
53. K. M. Kennedy, B. F. Kennedy, R. A. McLaughlin, and D. D. Sampson, "Needle optical coherence elastography for tissue boundary detection," Opt. Lett. **37**(12), 2310–2312 (2012).
54. W. Qi, R. Chen, L. Chou, G. Liu, J. Zhang, Q. Zhou, and Z. Chen, "Phase-resolved acoustic radiation force optical coherence elastography," J. Biomed. Opt. **17**(11), 110505 (2012).
55. J. P. Williamson, R. A. McLaughlin, W. J. Noffsinger, A. L. James, V. A. Baker, A. Curatolo, J. J. Armstrong, A. Regli, K. L. Shepherd, G. B. Marks, D. D. Sampson, D. R. Hillman, and P. R. Eastwood, "Elastic properties of the central airways in obstructive lung diseases measured using anatomical optical coherence tomography," Am. J. Respir. Crit. Care Med. **183**(5), 612–619 (2011).
56. R. Bu, S. Balakrishnan, H. Price, C. Zdanski, S. Mitran, and A. L. Oldenburg, "Localized compliance measurement of the airway wall using anatomic optical coherence elastography," Opt. Express **27**(12), 16751–16766 (2019).
57. J. Schmitt, "OCT elastography: imaging microscopic deformation and strain of tissue," Opt. Express **3**(6), 199–211 (1998).
58. A. Grimwood, L. Garcia, J. Bamber, J. Holmes, P. Woolliams, P. Tomlins, and Q. A. Pankhurst, "Elastographic contrast generation in optical coherence tomography from a localized shear stress," Phys. Med. Biol. **55**(18), 5515–5528 (2010).
59. V. Y. Zaitsev, A. L. Matveyev, L. A. Matveev, G. V. Gelikonov, V. M. Gelikonov, and A. Vitkin, "Deformation-induced speckle-pattern evolution and feasibility of correlational speckle tracking in optical coherence elastography," J. Biomed. Opt. **20**(7), 075006 (2015).
60. E. Li, S. Makita, S. Azuma, A. Miyazawa, and Y. Yasuno, "Compression optical coherence elastography with two-dimensional displacement measurement and local deformation visualization," Opt. Lett. **44**(4), 787–790 (2019).
61. R. A. Baldewsing, J. A. Schaar, F. Mastik, C. W. Oomens, and A. F. van der Steen, "Assessment of vulnerable plaque composition by matching the deformation of a parametric plaque model to measured plaque deformation," IEEE Trans. Med. Imaging **24**(4), 514–528 (2005).
62. C. Sun, B. Standish, and V. X. Yang, "Optical coherence elastography: current status and future applications," J. Biomed. Opt. **16**(4), 043001 (2011).
63. R. A. Baldewsing, C. L. de Korte, J. A. Schaar, F. Mastik, and A. F. van der Steen, "Finite element modeling and intravascular ultrasound elastography of vulnerable plaques: parameter variation," Ultrasonics **42**(1-9), 723–729 (2004).
64. M. M. Doyley, "Model-based elastography: a survey of approaches to the inverse elasticity problem," Phys. Med. Biol. **57**(3), R35–R73 (2012).
65. L. Dong, P. Wijesinghe, D. D. Sampson, B. F. Kennedy, P. R. T. Munro, and A. A. Oberai, "Volumetric quantitative optical coherence elastography with an iterative inversion method," Biomed. Opt. Express **10**(2), 384–398 (2019).
66. T. Ramanathan and H. Skinner, "Coronary blood flow," Continuing Education in Anaesthesia Critical Care & Pain **5**(2), 61–64 (2005).
67. V. Thondapu, C. V. Bourantas, N. Foin, I. K. Jang, P. W. Serruys, and P. Barlis, "Biomechanical stress in coronary atherosclerosis: emerging insights from computational modelling," Eur Heart J **38**, 81–92 (2016).
68. J. Ohayon, O. Dubreuil, P. Tracqui, S. Le Floc'h, G. Rioufol, L. Chalabreysse, F. Thivolet, R. I. Pettigrew, and G. Finet, "Influence of residual stress/strain on the biomechanical stability of vulnerable coronary plaques: potential impact for evaluating the risk of plaque rupture," Am J Physiol Heart Circ Physiol **293**(3), H1987–H1996 (2007).
69. B. Hinz, "Mechanical aspects of lung fibrosis: a spotlight on the myofibroblast," Proc. Am. Thorac. Soc. **9**(3), 137–147 (2012).
70. B. Emon, J. Bauer, Y. Jain, B. Jung, and T. Saif, "Biophysics of tumor microenvironment and cancer metastasis - a mini review," Comput. Struct. Biotechnol. J. **16**, 279–287 (2018).